

## Towards integrated nanoplasmonic logic circuitry

Cite this: DOI: 10.1039/c3nr00830d

Moshik Cohen,<sup>\*ab</sup> Zeev Zalevsky<sup>bc</sup> and Reuven Shavit<sup>a</sup>

Surface plasmon polaritons (SPPs) may serve as ultimate data processing expedients in future nanophotonic applications. SPPs combine the high localization of electrons with the bandwidth, frequency and propagation properties of photons, thus supplying nature with the best of two worlds. However, although plasmonics have recently gained constantly growing scientific attention, logic devices that operate on SPPs on a deep nanometer scale are yet to be demonstrated. Here, we design, fabricate and experimentally verify the smallest, first ever reported all optical nanoplasmonic XOR logic gate. The introduced XOR device is based on a novel engineerable interferometry scheme with extremely compact dimensions of  $\lambda^3/15\,500$ , which can be used to realize a variety of plasmonic logic functionalities. We use frequency modulated Kelvin probe microscopy to provide evidence of binary XOR functionality performed directly on SPPs with  $\lambda^3/80\,000$  mode volumes. An extinction ratio of 10 dB is achieved for a device length of 150 nm, increasing up to 30 dB for a device length of 280 nm. Our findings confirm plasmonics as the favorite data carriers in integrated all optical logic devices operating on the deep nanoscale, and pave the way to the development of future ultrafast information processing technologies based on SPPs.

Received 16th February 2013

Accepted 28th March 2013

DOI: 10.1039/c3nr00830d

[www.rsc.org/nanoscale](http://www.rsc.org/nanoscale)

## Introduction

With the rapidly growing demand for higher data processing rates, silicon based electronic devices approach fundamental speed and bandwidth limitations, which is an increasingly serious problem that impedes further progress in numerous fields of modern science and technology. These limitations arise from interconnect delays, and from increased power dissipation of transistors as their gate lengths approach a single-nanometer scale.<sup>1–4</sup> Possible solution for these setbacks may lay in photonics devices, as photons provide a considerably superior information bandwidth and improved thermal properties as compared to electrons.<sup>5,6</sup> Although semiconductor based optical devices had previously been introduced,<sup>7–10</sup> large-scale integration of photonic circuitry has been fundamentally limited by their large, diffraction limited size and by the poor optical response of silicon at optical frequencies. Recently, it has been suggested that surface plasmon nanophotonics may overcome these limitations.<sup>11–14</sup> Newly introduced plasmonic nanoantennae,<sup>14–17</sup> waveguides<sup>18–21</sup> and devices<sup>18,22–24</sup> unlock an enormous potential for exciting new applications based on SPPs. Predominantly, nanometric all optical logic devices that use plasmonics as data carriers, are of prime importance for future information processing and photonic computing

technologies. Still, although plasmonic based logic devices where recently introduced,<sup>10,25</sup> logic devices which operates directly on SPPs in deep nanoscale have not been reported. Recently, Lu *et al.* reported on Metal–Insulator–Metal (MIM) based plasmonic structures<sup>26–28</sup> which use highly confined modes to achieve miniaturization and high performances. Here, we design fabricate and characterize a novel, silicon based all optical nanoplasmonic exclusive or (XOR) gate. The device achieves smallest reported dimensions for plasmonic logic gate, which is three order of magnitude smaller than recently reported SPP logic devices<sup>10,25</sup> and therefore achieves significantly lower losses and smaller delay times. The logic operation is obtained by interference of SPPs through ultrathin Ag film with measured lateral dimensions of  $4 \times 20$  nm, achieving the smallest reported dimensions for all optical logic gate. Additional logic and Boolean functionalities can be realized by engineering the interferometer dimensions. We propose a special excitation and waveguiding scheme which facilitates the launch of nanometric SPPs from laser illumination and forces them towards the gate. High resolution (HR) atomic force microscopy (AFM) system with He–Ne laser at wavelength of 633 nm is used to excite and trace the nanoplasmonic waves along the structure and particularly at the device area. We theoretically and experimentally show full logic XOR functionality of the reported gate; with device operation at a broad frequency range enables multi tera-bits per second ( $\text{Tbit s}^{-1}$ ) data processing rates. The XOR logic device consists of two MIM waveguides separated by a 4 nm ( $\delta = 4$  nm) thick metallic layer.

The MIM waveguides comprising the nanoplasmonic interferometer are integrated with identical dielectric cores of two

<sup>a</sup>Department of Electrical and Computer Engineering, Ben-Gurion University of the Negev, Beer-Sheva 84105, Israel. E-mail: Moshik.Cohen80@gmail.com

<sup>b</sup>Faculty of Engineering, Bar-Ilan University, Ramat-Gan 52900, Israel

<sup>c</sup>Bar-Ilan Institute for Nanotechnology & Advanced Materials, Ramat-Gan 52900, Israel

independent MIM plasmonic waveguides. In the other perimeter of the system, the waveguides are connected to resonant dipole nanoantennae to achieve efficient excitation of propagating SPPs from laser illumination. To fabricate the nanoplasmonic devices, 20 nm Ag layer was sputtered on top of chemically cleaned wafers, *via* ion sputtering at vacuum levels of less than  $9e^{-7}$  Torr without cooling. The structures were patterned using gallium focused ion beam (Ga FIB) with 7 nm ion beam spot size. The acceleration voltage was set to 5 kV and currents as low as 0.69 nA were applied. Fig. 1b shows a SEM image of the fabricated nanometric interferometer, integrated with the plasmonic system. The silver structures are shown in bright colors, and the gray background represents the SOI substrate. We respectively mark the inputs and output to the device as “ $I_1$ ”, “ $I_2$ ” and “Out”. The overall area occupied by the nanoplasmonic gate with the excitation system is  $1 \times 1 \mu\text{m}$ , which is more than 200 times smaller as compared to the system reported in ref. 25 The average surface roughness measured on the internal faces of the system is 2 nm, obtained by experimental optimization of the lithography process.

The theoretical operation principle of the nanoplasmonic interferometer may be explained using the coupled modes theory,<sup>29</sup> which suggests that a structure built out of two identical slab waveguides with a sub-wavelength separation transfers light between the two waveguides with a constant phase shift of  $\pi/2$ . The spatial periodicity of the power transfer between the two MIM waveguides depends on the magnitude of the wave number  $k = 2\pi/\lambda_{\text{SPP}}$ , where  $\lambda_{\text{SPP}}$  is the wavelength of the propagating plasmonic mode within the waveguide.

In optical frequencies, the refractive index of metals can be expressed as  $n = n_i + jn_j$ , where the real part  $n_i$  governs the phase of a signal and the imaginary part  $n_j$  origins absorption. From the refractive index, we extract the relative permittivity by

$$\varepsilon = \varepsilon' + j\varepsilon'', \quad \varepsilon' = n_i^2 - n_j^2; \quad \varepsilon'' = 2n_in_j \quad (1)$$

where  $\varepsilon'$  and  $\varepsilon''$  are the real and imaginary part of  $\varepsilon$ , respectively. The thickness of the silver metallic layer is numerically designed to accomplish the relative phase shift of  $\pi$  between the plasmonic modes, which is required to realize XOR operation.<sup>30</sup> The MIM waveguides comprising the interferometer are integrated with identical dielectric cores of two independent MIM plasmonic waveguides. In the other perimeter of the system, the waveguides are connected to resonant dipole nanoantennae to achieve efficient excitation of propagating SPPs from laser illumination. It was recently observed excitation of MIM SPP waveguides using dipole nanoantennae achieves coupling efficiencies which are orders of magnitude higher as compared to direct illumination of a bare waveguide.<sup>31</sup> To achieve maximum excitation efficiency, we maximize the intensity of the electric field in the dipole gap, and simultaneously minimize the impedance mismatch between the dipole and the waveguide by geometry optimization. These requirements are met by maximization of the net power flowing through the waveguide cross-section, which also ensures flow of propagating SPPs towards the device. The net power flow is given by

$$W = \iint \text{Re} \left\{ \vec{P} \right\} \cdot \vec{n} \, dS \quad (2)$$

where  $\vec{P}$  is the Poynting vector for the propagating SPPs and  $\vec{n}$  is a vector in the direction of wave propagation. The dimensions of the nanoantennae are optimized to achieve maximum  $W$  in the MIM waveguides. The numerical analysis and optimization of the structures were carried out using finite element method (FEM) commercial SW package HFSS V14.<sup>32</sup> Fig. 2a shows the 3D electromagnetic model for analysis and optimization of the system. The model is comprised of Ag plasmonic nanostructures

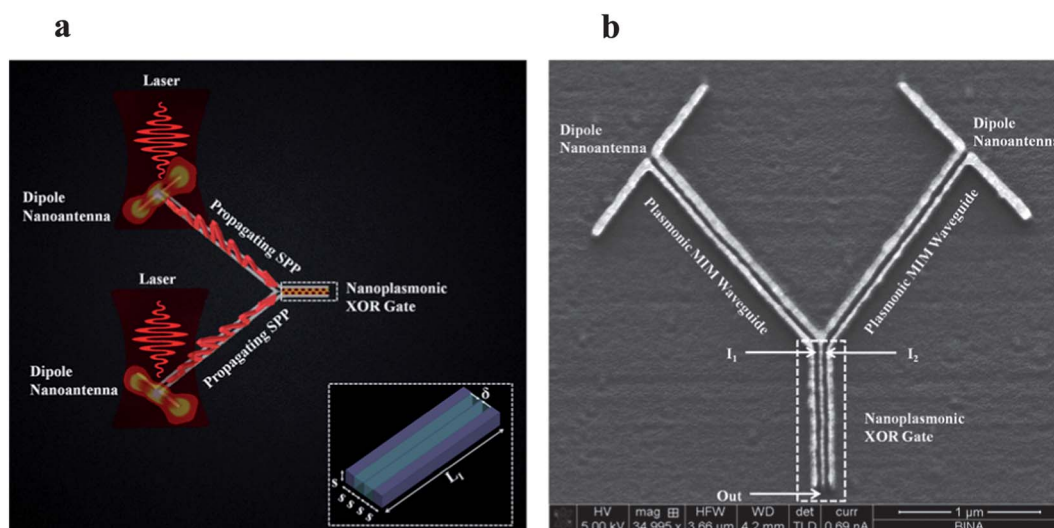


**Fig. 1** Nanoplasmonic interferometer based XOR gate integrated with SPP excitation and waveguiding system. (a) Schematic illustration of the reported nanoplasmonic system. Micron-scale optical excitation is converted to nano-scale plasmonic waves by the resonant dipole nanoantennae, confined and guided *via* plasmonic MIM waveguides towards the plasmonic XOR device, which performs the logic operation. The inset shows 3D illustration of the nanoplasmonic interferometer which used to realize XOR logic functionality.  $s = 20$  nm, the thickness of the internal metallic layer is  $\delta = 4$  nm and  $L_1 = 300$  nm represents the overall interferometer length. (b) SEM image of the fabricated nanoplasmonic system.

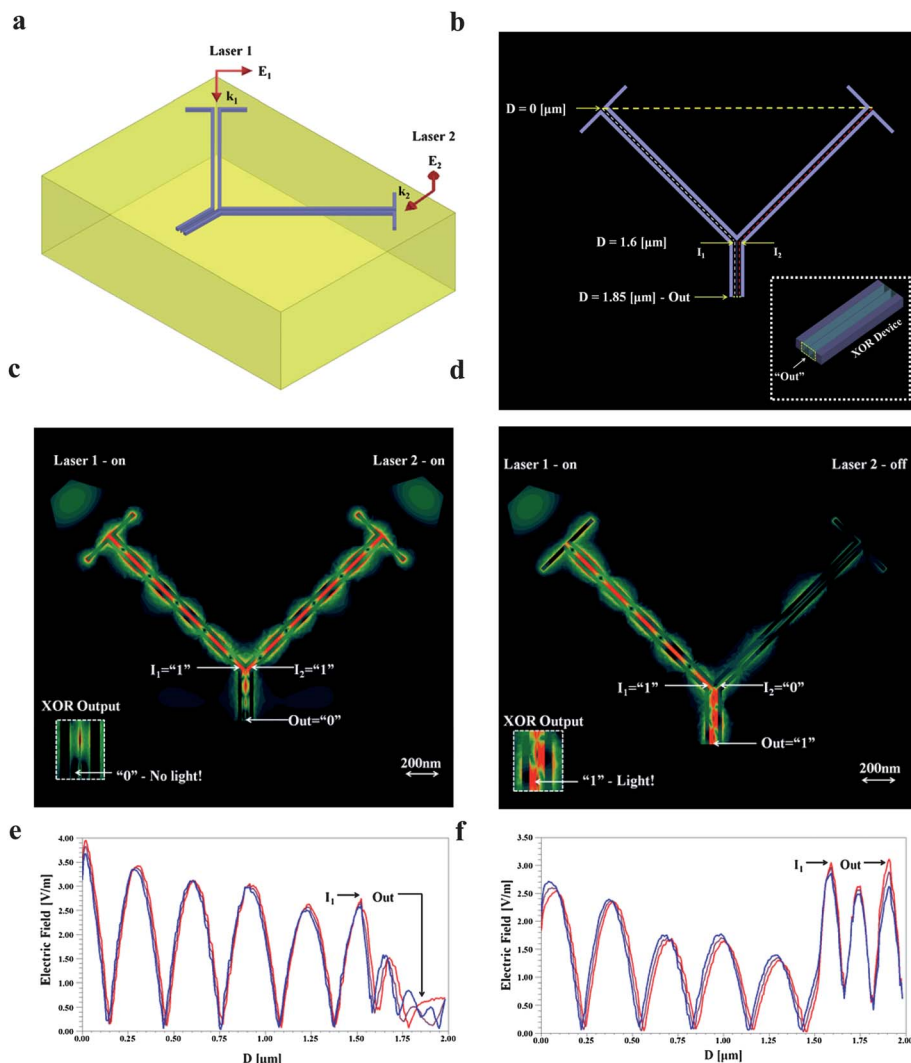


**Fig. 2** Theoretical analysis and design of the nanoplasmonic XOR gate and excitation system. (a) 3D EM model for the analysis and optimization of the nanoplasmonic device. (b) 2D description of the model. The graphs in Fig. 2e and f and Fig. 3b are plotted on white and red dashed lines defined here. The inset shows the nanoplasmonic device with definition for the location of the output signal. (c) 3D numerical calculation results of the system performance for XOR("1", "1") = "0", the device region is shown in the inset. (d) 3D numerical calculation results of the system performance for XOR("1", "0") = "1", the device region is shown in the inset. (e) Electric field magnitude along the system, for the case of XOR("1", "1"). The field is presented along the dashed line defined in Fig. 2b. The fields are plotted for three different phases of the laser excitation, as the red brown and blue patterns correspond to excitation phases of 45, 50 and 55°, respectively. (f) Electric field magnitude for XOR("1", "0"), plotted along the same geometry and for the same laser excitation phases as in Fig. 2e.

deposited on SOI substrate, while the materials properties are obtained from ref. 33

Each nanoantenna is illuminated by a laser at a wavelength of 1.55  $\mu\text{m}$ , linearly polarized in the dipole direction, and with a parameterized incident angle. Each laser beam is focused to a radius of 1  $\mu\text{m}$ , centered at the origin of the corresponding nanoantenna. Selectively dense meshing of a maximum 1 nm cell size was assigned at the metallic regions to precisely capture the plasmonic logic operation obtained by the device. The model was terminated by PML absorbing boundaries, matched to the material at the boundary of each computational domain. The convergence criterion was set to less than 1% energy variation between three successive iterations of adaptive mesh refinement. The results are presented at the optical frequency, *i.e.* 194.55 THz. The device output power is determined by integrating the time-

averaged power flow over the area which includes the cross-section of both waveguides. Thus, the device output, "Out", has dimensions which include the cross-section of the waveguides and separation layer, *i.e.*,  $44 \times 20$  nm, as shown in the inset of Fig. 2b. As defined in eqn (2), we use the net power flow to maximize the SPP coupling from the optical laser, thus to assure maximum transfer of voltage and current to the waveguide. The electric field magnitude, which is proportional to the power flow ( $P \propto |E|^2$ ), is used to describe the nanoplasmonic system performances, similar to recently reported works.<sup>34,35</sup> Fig. 2c shows the numerically calculated electric field magnitude for XOR("1", "1") = "0" logic operation, in which both nanoantennae are illuminated. The optical laser radiation is efficiently coupled to SPP modes that propagate through MIM waveguides toward the nanoplasmonic XOR device. Zoom in-to the area of the device

shows destructive plasmons interference, which results in logic zero ("0") at the output of the device, as emphasized in the inset. Fig. 2d illustrates XOR ("1", "0") = "1" logic operation, with zoom in-to the area of the device shown in the inset displaying the high field value which corresponds to logic "1". For this case, a portion of the propagating SPPs is reflected from the device input and coupled to the other waveguide. The intensity of the undesired reflected field is 20 dB lower as compared to that of the plasmon in the excited waveguide, *i.e.*  $S_{12} = -20$  dB. Full modulation, *i.e.* 30 dB extinction ratio at the device output, is achieved after less than 300 nm of interference length ( $L_1 < 300$  nm, as defined in Fig. 1a). This indicates on high speed phase accumulation through tunneling of the plasmonic modes, until a relative phase shift of  $\pi$  between the waveguides is accomplished. Fig. 2e and f show the electric field magnitude at the center of the MIM waveguide and the device for XOR ("1", "1") = "0" and XOR ("1", "1") = "1", respectively. The field is plotted along the white dashed line defined in Fig. 2b, for three different phases of the illuminating lasers. Fig. 2e shows the destructive interference results in logic "0" for the case of two active lasers. In Fig. 2f we observe similar electric field profiles at the input (located at  $D = 1.6$   $\mu\text{m}$ ) and output (located at  $D = 1.9$   $\mu\text{m}$ ) of the device, for logic level "1", which is an essential property for realization of logic gates. The numerical analysis for XOR ("0", "1") = "1" logic operation is presented in Fig. 3.

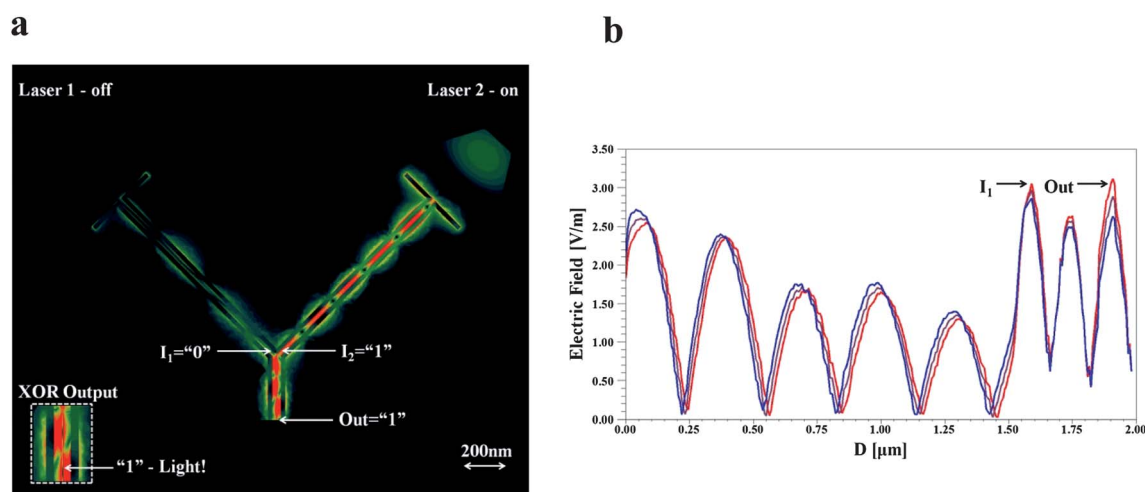
Fig. 3a illustrates XOR ("0", "1") = "1" logic operation, with zoom in-to the area of the device shown in the inset. Symmetrical field distributions are obtained, as expected from the symmetry of the analyzed geometry. Fig. 3b presents the electric field magnitude along the red dashed line described in Fig. 2b, for three different phases of the illuminating laser. We observe identical graphs to the results presented in Fig. 2f, as anticipated due to symmetry. The output signal can be extracted by connecting a coupling structure to the device output. The coupling structure shall have a minimum cross-section of  $20 \times 44$  nm to achieve identical output power for XOR ("1", "0") and XOR ("0", "1") logic states, which can be easily achieved using a

coupling grating structure<sup>25</sup> or plasmonic nanoantenna couplers.<sup>34</sup> Linear tapered MIM based nanofocusing can be used if additional confinement of the output signal is desired.<sup>34,36</sup>

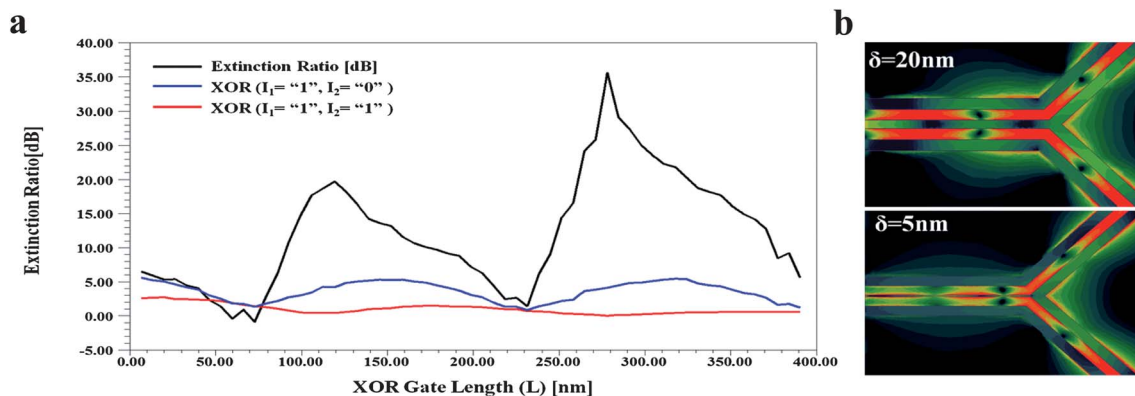
The black graph in Fig. 4a shows the extinction ratio *vs.* the interference length, as the blue and red curves are XOR ("1", "0") and XOR ("1", "1"), respectively. It is observed that the extinction ratio has two peaks, at  $L = 130$  nm and  $L = 280$  nm, corresponding to the peaks appearing in XOR ("1", "0"). An extinction ratio of 35 dB is obtained for  $L = 280$  nm; this high value is obtained due to strong destructive interference in XOR ("1", "1") response. The dependence of the power transfer as a function of the separation width was rigorously studied, for values between of  $\delta$  varying from 3 to 20 nm ( $\delta = S$ ). Fig. 4b shows the fields in the XOR device area for  $\delta = 20$  nm and for  $\delta = 5$  nm. We observe very low coupling between the waveguides for  $\delta = 20$  nm, yielding no destructive interference.

For  $\delta = 5$  nm the coupling between the waveguides is higher, which results in destructive interference and XOR ("1", "1") = "0" is accomplished. However, the observed "0" logic level achieved for  $\delta = 5$  nm is significantly higher than the "0" logic level in the optimal design ( $\delta = 4$  nm). The higher level of "0" results in degradation of the extinction ratio to a maximum of 12 dB, as compared to 35 dB for the optimal design.

We use the surface electric potential measurement in Frequency Modulated Scanning Kelvin Probe Microscopy (FM-SKPM) for experimental characterization of the reported nanoplasmonic structures. Surface potential microscopy measures the contact potential difference (CPD) between the scanning tip and the characterized device. Generally, CPD is highly material-dependent and related to the work functions of the pure material and to additional surface dipole moments.<sup>37</sup> The contribution of bulk and surface plasmons to the work functions of the materials<sup>38-42</sup> as well as to the van der Waals force<sup>43,44</sup> were previously reported. Our AFM system includes He-Ne laser at a wavelength of 633 nm which illuminates the entire sample to excite propagating SPPs from the nanoantennae gaps toward the XOR device. Fig. 5a presents a 2D



**Fig. 3** Numerical analysis XOR ("0", "1") logic state. (a) Numerical calculation results of the system performance for XOR ("0", "1") = "1", the device region is shown in the inset. (b) Electric field magnitude for XOR ("0", "1"), plotted along the red dashed line shown in Fig. 2b. The red brown and blue patterns respectively correspond to excitation phases of 45, 50 and 55°; similar to Fig. 2e.



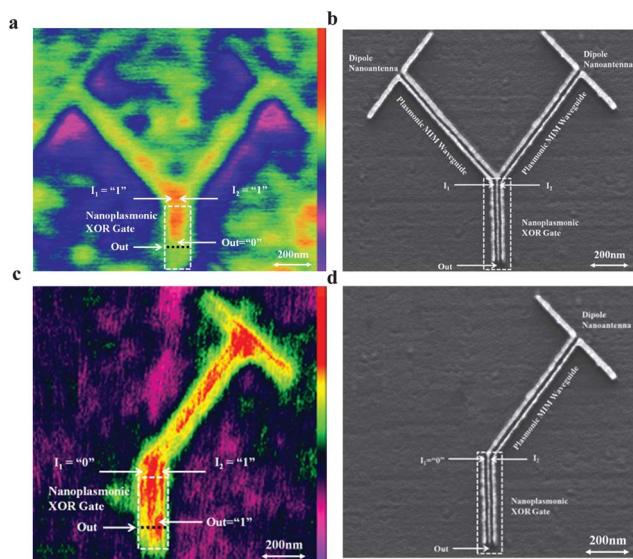
**Fig. 4** Extinction ratio and power transfer analysis. (a) Extinction ratio as a function of the device length. (b) Electric fields in the device region for XOR ("1","1") for  $\delta = 20$  nm (upper image) and for  $\delta = 5$  nm (lower image).

image of the surface electric potential on the sample for XOR ( $I_1 = '1', I_2 = '1'$ ) = "0" experiment, obtained for the structure shown in Fig. 5b. High field values are measured at both  $I_1$  and  $I_2$ , *i.e.*, "1". The XOR device realizes destructive interference between the SPPs at  $I_1$  and  $I_2$ , which results in low field values at the device output, *i.e.*, "0", as shown in Fig. 3b. Additional "hot spots" appear on the sample outside the plasmonic system. These "hot spots" represent localized surface plasmons excited by interaction of the laser light and residual Ag nanoparticles, which remained on the sample after the lithography process. We note that even though the laser illuminates the whole structure, the dominant effect which governs the device operation is caused by propagating SPPs from the nanoantennae. Therefore we neglect the effects caused by localized plasmons as well as by direct illumination of the device.<sup>35</sup> The ultrasmall

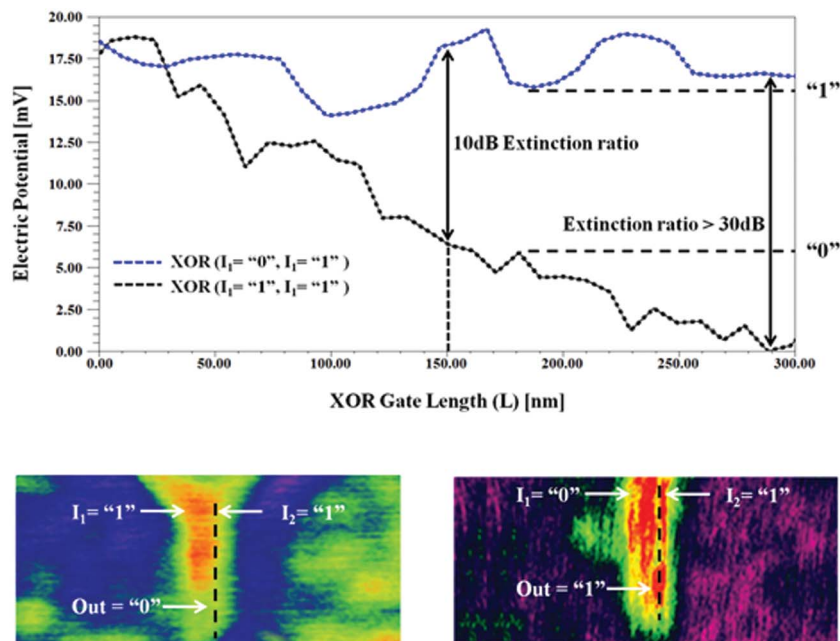
size of the introduced nanoplasmonic structures poses strong limitation on the capability to precisely confine the laser beam to separately excite each nanoantenna. Therefore, we fabricated an identical device integrated with a single nanoantenna and MIM waveguide, as shown in Fig. 5d. Fig. 5c shows the experimental results of XOR ( $I_1 = '0', I_2 = '1'$ ) = "1", obtained by characterization of the structure depicted in Fig. 5d. We observe low ("0") field values at  $I_1$ , and high field values ("1") at  $I_2$ . For this combination of inputs, the device yields high field values at the output "Out", as emphasized in Fig. 5d, resulting in XOR ("0","1") = "1". The reported nanoplasmonic gate implements a boolean XOR function on the propagating SPPs at inputs " $I_1$ " and " $I_2$ ". Hence, the signal level of "1" at the device output "Out" results if only one of the inputs to the gate is at logic level "1". Otherwise, logic "0" shall be measured at "Out".

Fig. 6a shows the measured surface electric potential along the device for XOR ( $I_1 = '1', I_2 = '1'$ ), and XOR ( $I_1 = '0', I_2 = '1'$ ). The fields are presented from the inputs to the gate ( $L = 0$ ) to the boundary of the physical device ( $L = 300$  nm), as a function of the distance,  $L$ . The quanta are presented along a dashed line as described in Fig. 6b. We define an electric potential at the output of  $>16$  mV as the "1" or 'ON' state, and potential  $<6$  mV as "0" or 'OFF' state. For the case of XOR ( $I_1 = '1', I_2 = '1'$ ), destructive interference between the plasmonic modes along the device leads to rapid attenuation of the signal which results in "0" logic level at the output, as shown in the black graph of Fig. 6a. For the case of XOR ( $I_1 = '0', I_2 = '1'$ ) the field maintains high level through the device, achieving "1" at the output, as shown in the blue graph of Fig. 6a.

The experimental results are summarized in Table 1, which is in perfect agreement with the true table of a XOR device. An extinction ratio of 10 dB between the logic levels at the device output is accomplished after only 150 nm, increasing up to 30 dB for a device length of 280 nm. The extremely small size of the device is achieved due to the introduced interferometry structure. Tunneling of the SPP modes through the nanometric separation layer leads to rapid phase accumulation, until a relative phase shift of  $\pi$  between the waveguides is accomplished. This architecture achieves the required phase accumulation much faster and after a smaller interference length as compared to the linear



**Fig. 5** Performance characterization of the nanoplasmonic logic XOR gate, integrated with the excitation and waveguiding system. (a) 2D measurement of XOR ("1","1") = "0" logic functionality. (b) HR SEM image of the fabricated structure for characterization of XOR ("1","1") = "0" logic functionality. (c) 2D measurement of XOR ("0","1") = "1" logic functionality. (d) HR SEM image of the fabricated structure for characterization of XOR ("0","1") = "1" logic functionality.



**Fig. 6** Measured electric potential along the nanoplasmonic XOR device. (a) The blue line represents the measured field for XOR ( $I_1 = '1', I_2 = '0'$ ) = "1". The black line represents the measured electric potential for XOR ( $I_1 = '1', I_2 = '1'$ ) = "0". Dashed points correspond to discrete measured values. The length of the XOR gate is defined by the interference length for which 10 dB extinction ratio is observed, *i.e.* 150 nm. (b) The line along which the fields are presented for the two experimental setups.

**Table 1** Experimental results at the output of the plasmonic logic XOR gate. Logic level of "1" at the inputs  $I_1$  and  $I_2$  is observed only when the corresponding nanoantenna is illuminated. 10 dB extinction ratio between the logic levels at the device output "Out" is obtained at a device length of 150 nm, increasing up to 30 dB for a device length of 280 nm

$I_1$	$I_2$	Out = XOR ( $I_1, I_2$ )
0	0	0
0	1	1
1	0	1
1	1	0

interference mechanism used in ref. 25, in which the phase accumulation is based on the propagation length. As a result, the reported XOR device is more than 3 orders of magnitude smaller

than in ref. 25. As micron scale plasmonic devices<sup>10,25</sup> suffer from high propagation loss, longer delay times and huge size mismatch with CMOS electronics; we propose the first nanoplasmonic architectural solution for these setbacks.

We provide further experimental evidence for the existence of propagating SPPs along the device, by observing the spatial frequency content of the measured fields on the sample. Since the gate exhibits imperfect impedance matching at its boundaries, partial standing waves are excited along the system. These standing waves are characterized by stationary spatial behavior, which is identical to the spatial frequency of the propagating SPPs and therefore can be detected *via* surface potential measurement in FM KPFM. To examine the spatial frequency content of the fields along the XOR gate, we performed spatial fast Fourier transform (FFT) on the surface electric potential

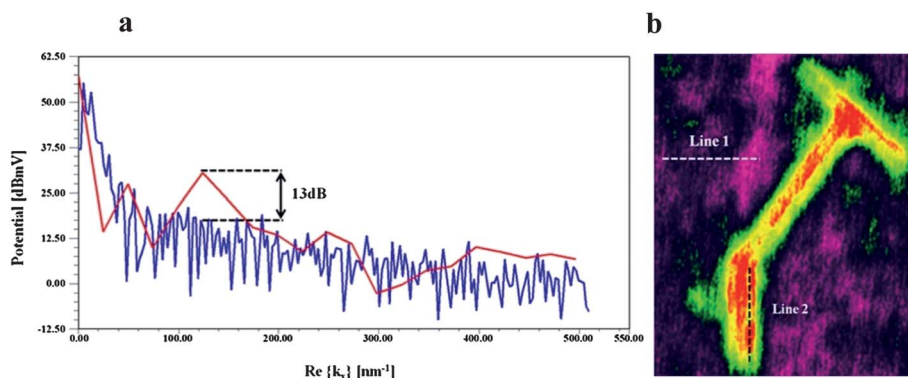


**Fig. 7** Spatial Fourier analysis of the measured surface electric potential on the sample. (a) The red curve shows the spatial FFT performed on the field along the XOR device, defined as "Line 2" in Fig. 7b. The blue curve presents spatial FFT analysis of the field outside the XOR device, performed on "Line 1" in Fig. 7b. (b) Definition of the lines on which we performed spatial FFT.

measured along the sample. Fig. 7a presents the spatial FFT results for two different measurements of the surface electric potential on the sample. The lines on which the FFT were calculated are detailed in Fig. 7b. The blue curve shows the spatial FFT of the surface potential along a line, which is outside the device (Line 1 in Fig. 7b), as the red curve is the spatial FFT of the surface potential along the center of the device (Line 2 in Fig. 7b). For both measurements shown in Fig. 7a the dominant field component appears at low spatial frequencies, a result which is in good agreement with the general electrostatic character of the measured potential and is due to the standing waves in the structure. However, we observe a strong spatial frequency component in the field along the device, at  $\text{Re}\{k_{\text{SPP}}\} = 125 \mu\text{m}^{-1}$ . The amplitude of this component is 13 dB higher than the corresponding component in the measurement described by the blue curve. This result confirms the existence of propagating SPPs with wave vector of  $\text{Re}\{k_{\text{SPP}}\} = 125 \mu\text{m}^{-1}$  inside the device, which is in excellent agreement with Dione *et al.*<sup>20</sup> and Chen *et al.*,<sup>45</sup> Thus further substantiates our theoretical analysis and experiments.

In this work we propose as well as validate theoretically and experimentally for the first time, the capability to compress all optical logic devices into volumes smaller than  $\lambda^3/15\,500$ . By employing extremely confined SPPs as information carriers in optical frequencies, the reported nanoplasmonic binary XOR gate exhibits the speed and bandwidth performances of photonics, with dimensions of integrated electronics. An extinction ratio of 10 dB is measured at the output for a device length of 150 nm, rising up to 30 dB for a device length of only 280 nm. The introduced interferometry architecture can be used to realize a variety of plasmonic logic functionalities in deep nanoscale. Our findings provide a path for the development of novel silicon nanophotonic processing circuits, achieving multi Tbit  $\text{s}^{-1}$  data processing rates with large-scale integration capabilities.

## References

- J. A. Schuller, E. S. Barnard, W. Cai, Y. C. Jun, J. S. White and M. L. Brongersma, *Nat. Mater.*, 2010, **9**, 193–204.
- E. Ozbay, *Science*, 2006, **311**, 189–193.
- J. A. Dionne, L. A. Sweatlock, M. T. Sheldon, A. P. Alivisatos and H. A. Atwater, *IEEE J. Sel. Top. Quantum Electron.*, 2010, **16**, 295–306.
- M. L. Brongersma and V. M. Shalaev, *Science*, 2010, **328**, 440–441.
- R. Kirchain and L. Kimerling, *Nat. Photonics*, 2007, **1**, 303–305.
- N. Engheta, *Science*, 2007, **317**, 1698–1702.
- V. R. Almeida, C. A. Barrios, R. R. Panepucci and M. Lipson, *Nature*, 2004, **431**, 1081–1084.
- C. Koos, P. Vorreau, T. Vallaitis, P. Dumon, W. Bogaerts, R. Baets, B. Esembeson, I. Biaggio, T. Michinobu, F. Diederich, W. Freude and J. Leuthold, *Nat. Photonics*, 2009, **3**, 216–219.
- L. Bi, J. Hu, P. Jiang, D. H. Kim, G. F. Dionne, L. C. Kimerling and C. A. Ross, *Nat. Photonics*, 2011, **5**, 758–762.
- H. Wei, Z. Wang, X. Tian, M. Käll and H. Xu, *Nat. Commun.*, 2011, **2**, 387.
- M. Schnell, A. García-Etxarri, A. J. Huber, K. Crozier, J. Aizpurua and R. Hillenbrand, *Nat. Photonics*, 2009, **3**, 287–291.
- A. G. Curto, G. Volpe, T. H. Taminiau, M. P. Kreuzer, R. Quidant and N. F. van Hulst, *Science*, 2010, **329**, 930–933.
- S. Lal, S. Link and N. J. Halas, *Nat. Photonics*, 2007, **1**, 641–648.
- A. Kinkhabwala, Z. Yu, S. Fan, Y. Avlasevich, K. Müllen and W. E. Moerner, *Nat. Photonics*, 2009, **3**, 654–657.
- T. Kosako, Y. Kadoya and H. F. Hofmann, *Nat. Photonics*, 2010, **4**, 312–315.
- T. Shegai, S. Chen, V. D. Miljković, G. Zengin, P. Johansson and M. Käll, *Nat. Commun.*, 2011, **2**, 481.
- T. Pakizeh and M. Käll, *Nano Lett.*, 2009, **9**, 2343–2349.
- S. I. Bozhevolnyi, V. S. Volkov, E. Devaux, J.-Y. Laluet and T. W. Ebbesen, *Nature*, 2006, **440**, 508–511.
- J. R. Krenn, *Nat. Mater.*, 2003, **2**, 210–211.
- J. A. Dionne, L. A. Sweatlock, H. A. Atwater and A. Polman, *Phys. Rev. B: Condens. Matter Mater. Phys.*, 2006, **73**, 035407.
- R. F. Oulton, V. J. Sorger, D. A. Genov, D. F. P. Pile and X. Zhang, *Nat. Photonics*, 2008, **2**, 496–500.
- P. Berini and I. D. Leon, *Nat. Photonics*, 2011, **6**, 16–24.
- H. Yan, X. Li, B. Chandra, G. Tulevski, Y. Wu, M. Freitag, W. Zhu, P. Avouris and F. Xia, *Nat. Nanotechnol.*, 2012, **7**, 330–334.
- N. I. Zheludev, *Nat. Nanotechnol.*, 2010, **5**, 10–11.
- Y. Fu, X. Hu, C. Lu, S. Yue, H. Yang and Q. Gong, *Nano Lett.*, 2012, **12**, 5784–5790.
- H. Lu, X. Liu, Y. Gong, D. Mao and L. Wang, *Opt. Express*, 2011, **19**, 12885–12890.
- H. Lu, X. Liu, G. Wang and D. Mao, *Nanotechnology*, 2012, **23**, 444003.
- H. Lu, X. Liu, D. Mao and G. Wang, *Opt. Lett.*, 2012, **37**, 3780–3782.
- A. Yariv, *IEEE J. Quantum Electron.*, 1973, **9**, 919–933.
- O. Limon and Z. Zalevsky, *Opt. Eng.*, 2009, **48**, 064601.
- A. Andryieuski, R. Malureanu, G. Biagi, T. Holmgaard and A. Lavrinenko, *Opt. Lett.*, 2012, **37**, 1124–1126.
- V. G. Kravets, G. Zorinians, C. P. Burrows, F. Schedin, A. K. Geim, W. L. Barnes and A. N. Grigorenko, *Nano Lett.*, 2010, **10**, 874–879.
- Marvin J. Weber, *Handbook of Optical Materials*, CRC Press Book, 2003.
- M. Schnell, P. Alonso-González, L. Arzubiaga, F. Casanova, L. E. Hueso, A. Chuvilin and R. Hillenbrand, *Nat. Photonics*, 2011, **5**, 283–287.
- J. Wen, S. Romanov and U. Peschel, *Opt. Express*, 2009, **17**, 5925–5932.
- H. Choo, M.-K. Kim, M. Staffaroni, T. J. Seok, J. Bokor, S. Cabrini, P. J. Schuck, M. C. Wu and E. Yablonovitch, *Nat. Photonics*, 2012, **6**, 838–844.
- M. Nonnenmacher, M. O'Boyle and H. K. Wickramasinghe, *Ultramicroscopy*, 1992, **42–44**, 268–273, Part 1.
- R. Mehrotra and J. Mahanty, *J. Phys. C: Solid State Phys.*, 1978, **11**, 2061–2064.

- 39 F. A. Gutierrez, J. Díaz-Valdés and H. Jouin, *J. Phys.: Condens. Matter*, 2007, **19**, 326221.
- 40 F. J. García de Abajo, *Nucl. Instrum. Methods Phys. Res., Sect. B*, 1995, **98**, 445–449.
- 41 I. Brodie, *Phys. Rev. B: Condens. Matter*, 1995, **51**, 13660–13668.
- 42 M. Schmeits and A. Lucas, *Surf. Sci.*, 1977, **64**, 176–196.
- 43 E. Gerlach, *Phys. Rev. B: Solid State*, 1971, **4**, 393–396.
- 44 N. R. Hill, M. Haller and V. Celli, *Chem. Phys.*, 1982, **73**, 363–375.
- 45 J. Chen, G. A. Smolyakov, S. R. Brueck and K. J. Malloy, *Opt. Express*, 2008, **16**, 14902–14909.